

## Article

# Pyritization and Preservation Model of Chrysophyte Cyst Fossils in Shales during the Triassic Carnian Pluvial Episode, Ordos Basin, China: Evidence from Cyclostratigraphy, Radiometric Dating and Geochemical Analyses

Jingjing Cao <sup>1,2</sup>, Wenzhe Gang <sup>1,2,\*</sup> and Shangru Yang <sup>3</sup>

<sup>1</sup> State Key Laboratory of Petroleum Resources and Prospecting, China University of Petroleum, Beijing 102249, China; jingjingcao95@163.com

<sup>2</sup> College of Geosciences, China University of Petroleum, Beijing 102249, China

<sup>3</sup> Oil and Gas Technology Research Institute, PetroChina Changqing Oilfield Company, Xi'an 710018, China; yangshangru1992@163.com

\* Correspondence: gwz@cup.edu.cn

**Abstract:** Chrysophyte cyst fossils were widely pyritized and preserved in black shales from the seventh member (Ch7 Mbr) of the Yanchang Formation in the Ordos Basin. The age, pyritization, and preservation model of these fossils have not been studied previously. In this study, the astronomical orbital cycles of the Ch7 Mbr were determined based on the gamma ray series of the Yan56 and Zhen 421 wells. An astronomical time scale (ATS) analysis revealed that the depositional duration of Ch7 Mbr was approximately 5 Ma. According to the <sup>206</sup>Pb/<sup>238</sup>U radiometric dating of zircons using laser ablation inductively coupled plasma mass spectrometry (La-ICP-MS), the tuffs at the bottom of Ch7 Mbr were crystallized at 234 Ma, which served as a geological anchor. The ages of three submembers in Ch7 Mbr were estimated at 234.0–232.4 Ma, 232.4–230.8 Ma, and 230.8–229.1 Ma based on ATS analysis. In addition, chrysophyte cyst fossils were well preserved by pyritization in the Ch7 Mbr black shales. There were six types of microscopic morphologies with different pores, collars, and surface ornamentation under scanning electron microscopy (SEM). The age of the chrysophyte cyst fossils was at least 233.6 Ma in the Triassic Carnian Pluvial Episode (CPE) based on the 405 kyr tuned ATS. Moreover, the paleoredox conditions in Ch7 Mbr were reconstructed, and a preservation model of chrysophyte cyst fossils was established based on geochemical analyses. Fossil pyritization was caused by bacterial sulfate reduction near the water-sediment interface under suboxic to anoxic environmental conditions. Pyritization was initiated on the walls of the chrysophyte cysts by the formation of microcrystalline pyrite. Because of the gradual pyritization of the chrysophyte cyst wall, the organic matter in the interior of the fossil was well preserved.



**Citation:** Cao, J.; Gang, W.; Yang, S. Pyritization and Preservation Model of Chrysophyte Cyst Fossils in Shales during the Triassic Carnian Pluvial Episode, Ordos Basin, China: Evidence from Cyclostratigraphy, Radiometric Dating and Geochemical Analyses. *Minerals* **2023**, *13*, 991. <https://doi.org/10.3390/min13080991>

Academic Editor: Olev Vinn

Received: 8 June 2023

Revised: 22 July 2023

Accepted: 24 July 2023

Published: 26 July 2023

**Keywords:** chrysophyte cyst; pyritization; cyclostratigraphy; Triassic Carnian Pluvial Episode; Yanchang Formation; Ordos Basin

## 1. Introduction

Chrysophytes are primarily freshwater algae that produce siliceous cysts (termed statospores, resting spores, or stomatocysts) during their resting stages [1,2]. Chrysophyte cysts can be well-preserved in sediments as microfossils [3–6]. Because of their small size, scanning electron microscopy (SEM) has been used to overcome the limitations of low-resolution optical microscopy in observing microfossils [2–4,7]. Chrysophyte cysts naming and classification are based on their characteristic shapes, pores [4], collars [4], and ornamentation [8] observed under SEM [3]. Chrysophyte cysts are generally indicators of environmental reconstruction in modern lake sediments [9,10]. Zhang et al. (2016) were the first to report and describe the morphological characteristics of the chrysophyte cyst fossils in the Triassic Yanchang Formation in the Ordos Basin [8]. However, the preservation



**Copyright:** © 2023 by the authors. Licensee MDPI, Basel, Switzerland. This article is an open access article distributed under the terms and conditions of the Creative Commons Attribution (CC BY) license (<https://creativecommons.org/licenses/by/4.0/>).

conditions of chrysophyte cyst fossils have not yet been studied. In this study, we determined the age of chrysophyte cyst fossils based on the  $^{206}\text{Pb}/^{238}\text{U}$  isotopic age of zircons and cyclostratigraphic analysis. Furthermore, we meticulously described the microscopic morphologies and pyritization of chrysophyte cysts using optical microscopy and SEM. Finally, we reconstructed the paleoredox conditions of the shales based on geochemical parameters and established a model that describes the preservation of chrysophyte cysts.

## 2. Geologic Setting

The study area was situated in the southwestern Ordos Basin (Figure 1), which is the second-largest petroliferous basin in China [11]. It consists of the Yishan Slope, Jinxi Fault-fold Belt, Yimeng Uplift, Western Thrust Belt, Tianhuan Depression, and Weibei Uplift [12] (Figure 1A). The study area is located in the eastern part of the Western Thrust Belt and the northern part of the Weibei Uplift (Figure 1B). The Triassic Yanchang Formation in the Ordos Basin is an important formation known for its oil-gas accumulation and consists of terrigenous clastic rock deposits dominated by fluvial and lacustrine facies, with a thickness of approximately 1000 m [13,14] (Figure 2). According to the lacustrine evolution and cyclical lithological characteristics, the Yanchang Formation can be divided into 10 lithologic units, labeled from top to bottom as the first (Ch1) to tenth (Ch10) members (Mbr), with the seventh member (Ch7 Mbr) being a key section (Figure 2). The Yanchang Formation contains records of the entire process of the formation, development, and extinction of the lake basin, which is characterized by terrigenous clastic sedimentary rocks of the fluvial, delta, and lake facies [15]. Ch10 Mbr was river sediments, characterized by fine sandstones and mudstones. The depositional period from Ch9 Mbr to Ch8 Mbr was a lacustrine expansion stage, with a lithology of primarily mudstones and black shales [15]. At the beginning of the Ch7 Mbr, the lake water level reached its maximum depth, and thick black shales were deposited [16]. The lake basin began to decrease during the deposition of Ch6, transforming the lithology of Ch7 Mbr from black shale to mudstone, siltstone, and sandstone [17] (Figure 2). Ch4 and Ch5 Mbrs were composed of deltas and shallow lake sediments with mudstone and sandstone. During the deposition period of Ch3 to Ch1 Mbrs, the lake basin shrank and gradually disappeared, and the depositional environments changed from a shallow lake to a river [15–17] (Figure 2). In addition, tuff interlayers were formed by the deposition of volcanic eruption materials. Tuff was widely deposited at the bottom of Ch7 Mbr and served as a significant marker bed in the study area [16,17].

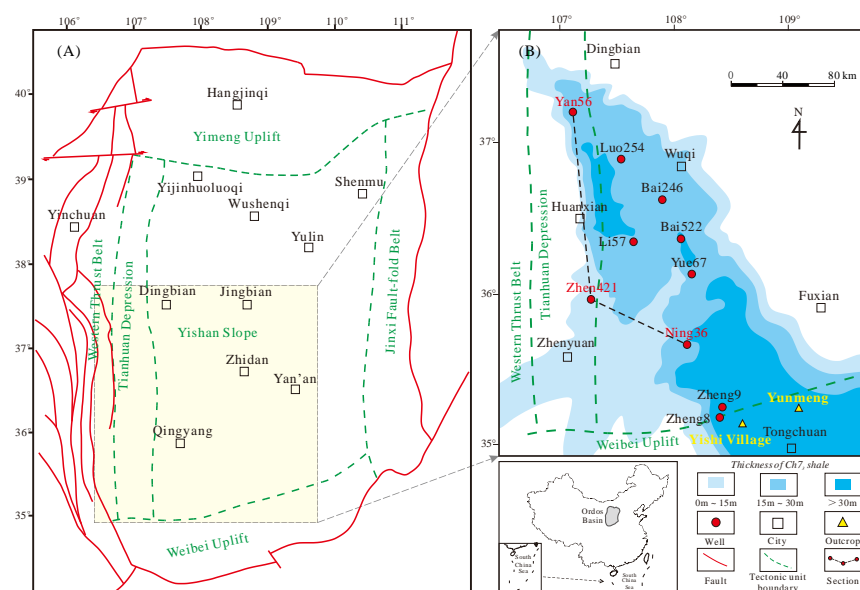


**Figure 1.** Tectonic unit division map (A) [18], location of the wells, and thickness of the shales of the Ch7 Mbr (B) in the Yanchang Fm., Ordos Basin, China [8].

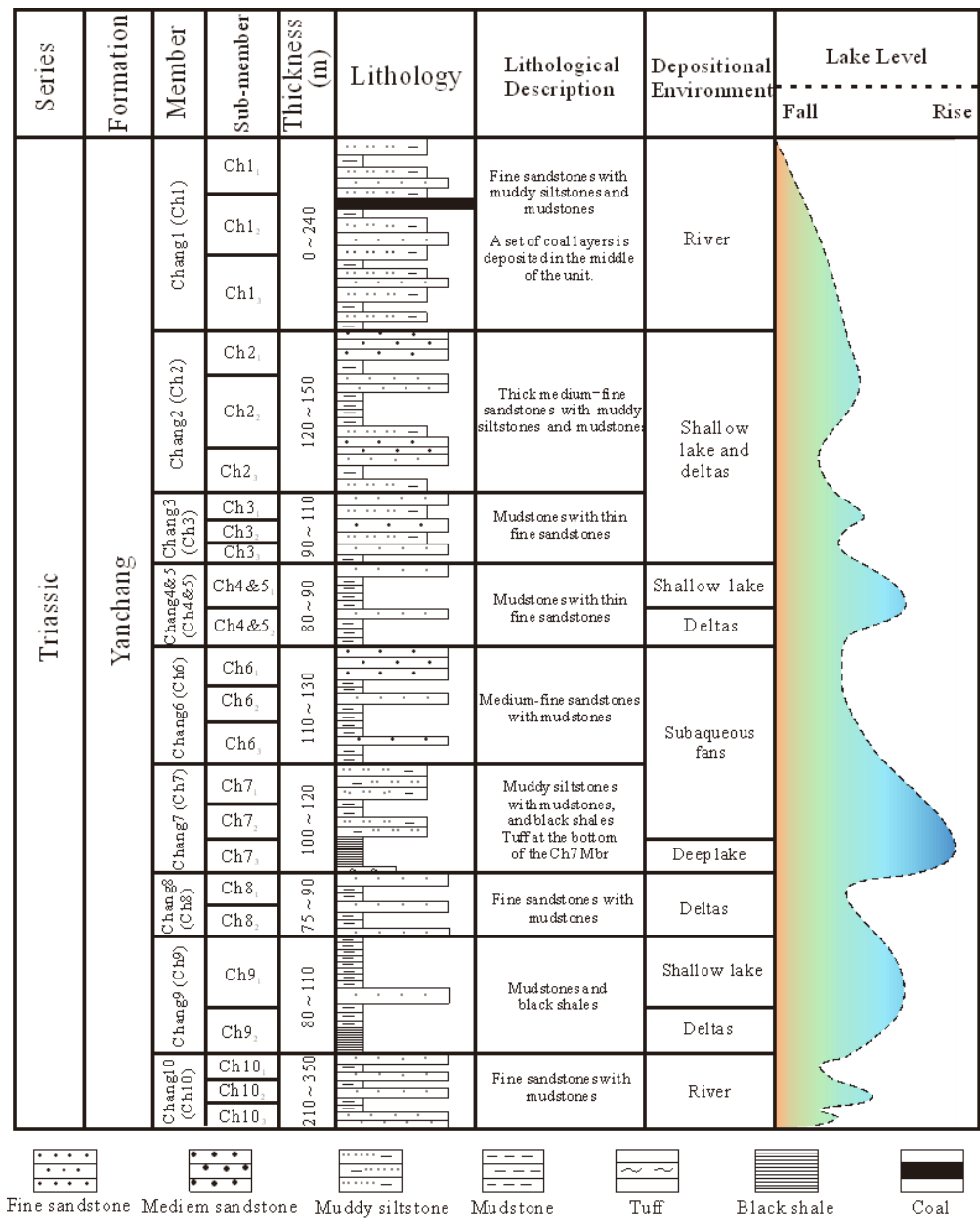


**Figure 2.** Stratigraphic column, depositional environment, and lake level in the Ch7 Mbr of the Yanchang Fm. in the Ordos Basin (modified from Chen et al., 2019) [19].

### 3. Materials and Methods

#### 3.1. Natural Gamma Ray (GR) Logging and Cyclostratigraphic Analysis

The values of natural gamma ray logging mainly originated from potassium (K), uranium (U), and thorium (Th) responses, which act as paleoclimatic proxies [20,21]. GR logging is sensitive to lithologic changes, and the logging curve interval was 0.125 m. Furthermore, GR data are vertically continuous and have high resolution, making them good proxies for paleoclimatic changes [21,22]. The GR data of Ch7 Mbr in Yan56 and Zhen421 were selected for cyclostratigraphy analysis to identify Milankovitch cycles using the *Acycle 2.0* software [21].

The detailed steps of the cyclostratigraphic analysis are presented below. First, abnormal values in the GR curve were removed, and linear interpolation was performed at an interval of 0.125 m [22]. Second, the locally weighted regression method (LOWESS) was used to remove the trend of GR data using a “LOWESS smoother” (smoother = 20%) [23]. The third step consisted of a spectral analysis using periodograms and red noise tests.

The existence of Milankovitch cycles in sedimentary strata was generally identified by frequency peaks with a confidence level greater than 95%. The fourth step included a Gaussian bandpass filter analysis using the dominant frequency as an input to obtain the filtering results [21].

### 3.2. SEM Observation and Energy-Dispersive Spectroscopy (EDS) Analysis

Chrysophyte cyst fossils were discovered in the black shales of Ch7 Mbr studied by Zhang et al. (2016) and in different wells [8]. The locations of the wells from which some of the chrysophyte cyst fossils were preserved are shown in Figure 1B. Chrysophyte cyst fossils were observed using optical microscopy, field-emission SEM, and EDS. The shales for SEM observation were prepared in two different ways: (1) samples were manually broken without polishing to identify chrysophyte cysts, and (2) samples were polished to obtain clear interior details of the chrysophyte cysts [8]. The SEM images were obtained using a Quanta 200F field-emission instrument at the Microstructure Laboratory for Energy Materials, China University of Petroleum (Beijing, China). EDS was used to measure the elemental content of pyrite in the chrysophyte cysts [18].

### 3.3. TOC and TS Analysis

Bulk geochemical analysis was carried out in the shales of the Ch7 Mbr in well Yan56. The total organic carbon content (TOC, wt.%) of 72 shale samples and total sulfur contents (TS, wt.%) of 88 shale samples were collected from previous studies [24–26]. Before measuring the contents of TOC and TS, the samples were crushed to 100 mesh, treated with 10% dilute hydrochloric acid, heated at 60 °C for 1 h to 2 h until carbonate minerals were completely removed, washed with distilled water, and dried for 10 h in an oven at 50 °C [27]. The TOC and TS contents were measured using a Leco CS-230HC carbon and sulfur analyzer at the State Key Laboratory of Petroleum Resources and Prospecting, China University of Petroleum (Beijing).

### 3.4. Carbon, Nitrogen, and Sulfur Isotopic Analysis

The organic carbon isotopes ( $\delta^{13}\text{C}_{\text{org}}$ , ‰) and nitrogen isotopes ( $\delta^{15}\text{N}$ , ‰) of 34 shale samples and sulfur isotopes ( $\delta^{34}\text{S}$ , ‰) of 59 shale samples were collected from previous studies [23–25,27]. The samples were crushed to 80 mesh and dissolved in diluted hydrochloric acid (1 mol/L) until the carbonate minerals were completely removed. The acidified samples were rinsed five to six times with deionized water and centrifuged after each rinse to minimize the loss of fine organic debris and clay from the sample material. The samples were then dried in an oven at 50 °C for 24 h and transferred to plastic tubes for storage until isotope analyses [24,26].

The  $\delta^{13}\text{C}_{\text{org}}$  values were obtained using a Flash HT EA-MAT 253 isotope ratio mass spectrometer (IRMS) at the State Key Laboratory of Petroleum Resources and Prospecting (SKLPRP), China University of Petroleum (Beijing) [28]. The  $\delta^{15}\text{N}$  values were measured using tin capsules in a Costech ECS 4010 combustion elemental analyzer coupled to a Thermo Finnigan Delta Plus IRMS [26]. The  $\delta^{34}\text{S}$  values were analyzed using a Flash 2000 EA-Delta V Plus IRMS at the Analytical Laboratory of the Beijing Research Institute of Uranium Geology (Beijing, China) [27].

### 3.5. Major and Trace Element Analysis

The concentrations of major and trace elements in 73 shale samples from well Yan56 were collected from previous studies [24–26,28]. Fresh shale core samples were ground using an agate mortar until the powder samples were finer than 200 mesh. The major element concentrations were determined using an AB104L Axiosm AX X-ray fluorescence spectrometer at the SKLPRP, China University of Petroleum (Beijing) [25]. The analytical errors of the major element concentrations were lower than 8%, according to duplicate analysis. Trace element concentrations were analyzed using a NexION300D ICP-MS (Element XR) at the SKLPRP, China University of Petroleum (Beijing) [24,29]. Powder

samples were treated with 1 mL HF and 0.5 mL HNO<sub>3</sub> digestion solution in a screw-top PTFE-lined stainless-steel bomb toasted in an oven at 190 °C for 24 h [29]. The insoluble residues were dissolved at 130 °C in 5 mL 30% (v/v) HNO<sub>3</sub> for 3 h [25,29]. The analytical errors in the trace element concentrations were less than <5%. The enrichment factors of uranium ( $U_{EF}$ ) were calculated using the equation  $X_{EF} = [(X/Al)_{sample}/(X/Al)_{PAAS}]$ , where X and Al represent the concentrations of X and aluminum (Al), respectively [30]. The samples were normalized using the average Post-Archean Australian shale (PAAS) [31].

## 4. Results

### 4.1. Spectral Analysis and Floating Astronomical Scale

The power spectra of the GR series of the Ch7 Mbr from the Yan56 well showed prominent peaks of 9.26–5.10 m, 2.29–1.27 m, and 0.91–0.63 m (Figure 3A). In addition, the power spectra of the GR series of the Zhen421 well exhibited distinct peaks of 8.89–5.82 m, 1.99–1.26 m, and 0.90–0.68 m above the 99% confidence level (Figure 3B). The peaks of the two wells are close to the ratio of long eccentricity (E), short eccentricity (e), and obliquity (O) (E:e:O = 20:5:2), which is similar to the theoretical cycles of the Middle Triassic [32]. Thus, the evidence of Milankovitch cycles existed in the sedimentary strata of the Ch7 Mbr of the Yanchang Fm. Generally, the long eccentricity obtained from the GR series of the Yan56 and Zhen421 wells was the most stable orbital parameter. Additionally, 405 kyr filtering of the GR series was combined with Gaussian passbands of  $0.110 \pm 0.022$  and  $0.118 \pm 0.023$  for the Yan56 and Zhen421 wells, respectively (Figure 4A). The long eccentricity cycles were numbered E1 to E13 from the bottom to the top of the Ch7 Mbr, which is consistent with the results of the magnetic susceptibility data of Ch7 Mbr from the Y1011 well [21] (Figure 4A). As each long eccentricity represented 405 kyr, chrysophyte cysts were discovered at the top of E1 (at least 233.6 Ma) (Figure 4A,B).

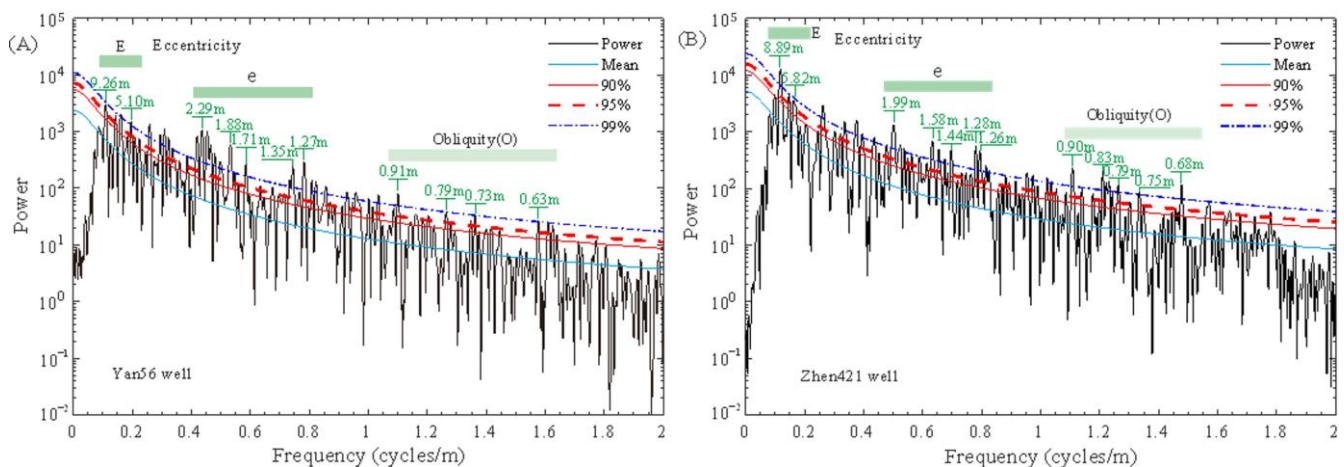


**Figure 3.** Power spectra of the GR series of the Ch7 Mbr from the wells (A) Yan56 and (B) Zhen421 in the Yanchang Fm., Ordos Basin.

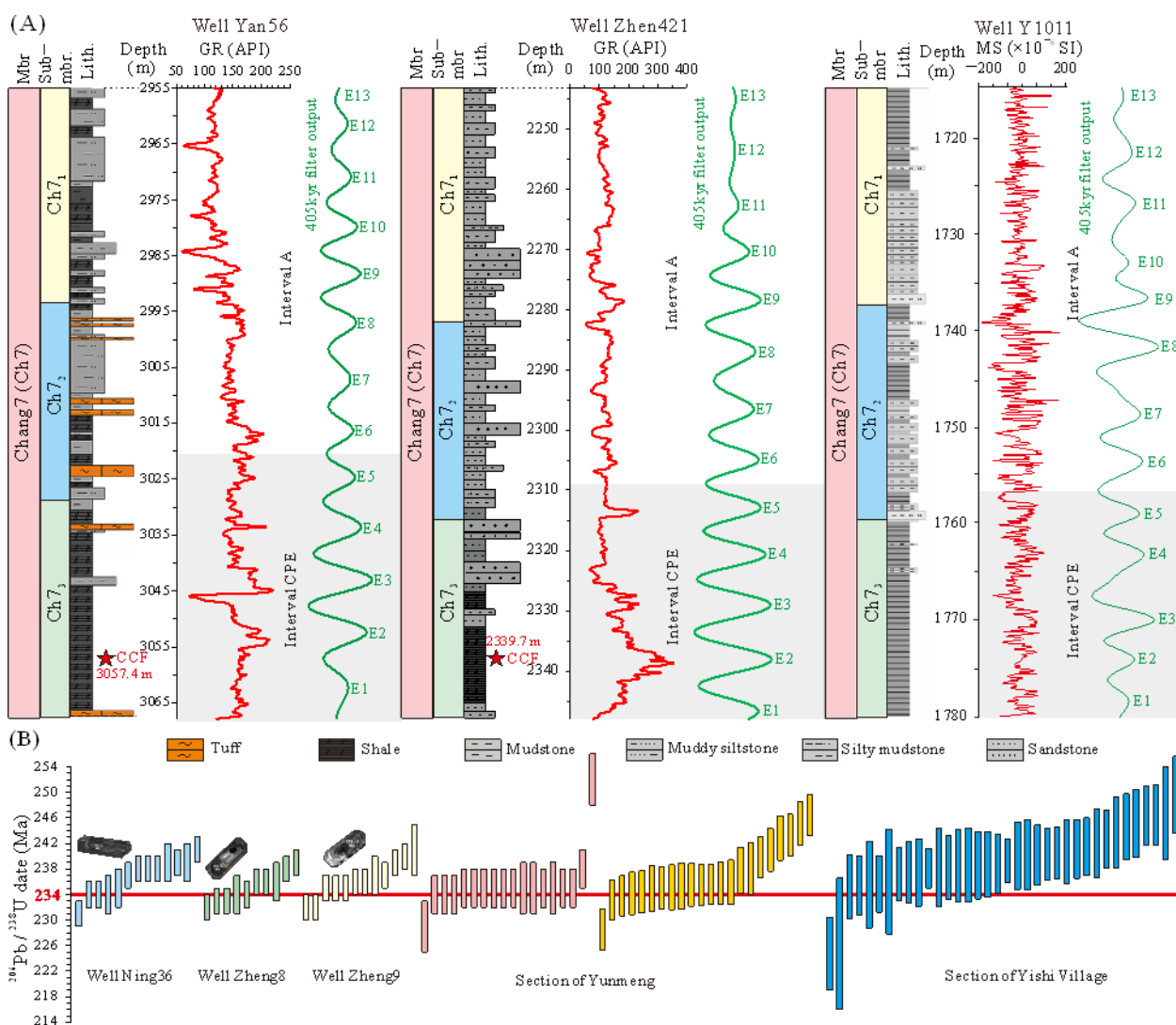


**Figure 4.** (A) Representative stratigraphic columns and long eccentricity (E: 405 kyr) filter outputs of the Yanchang Fm. in wells Yan56, Zhen421, and Y1011 [23]; (B) the  $^{206}\text{Pb}/^{238}\text{U}$  isotopic age of zircons in the tuffs at the bottom of the Ch7 Mbr of the Yanchang Fm. [33,34]. CCF represents the chrysophyte cyst fossil.

#### 4.2. TOC and TS Contents

The Carnian Pluvial Episode (CPE) was an important period of global climate spanning from 232 to 234 Ma [35,36]. According to the astronomical time scale (ATS) of the Ch7 Mbr established in this study, the samples from well Yan56 were sub-divided into two intervals: interval CPE (age: 232–234 Ma) and interval A (age: 229–232 Ma). The TOC content of interval A ranged from 0.68% to 7.40%, with an average value of 4.38%. The TOC content of interval CPE ranged from 1.93% to 9.7%, with an average of 5.60%, which is considered high. The TS values ranged from 0.05% to 5.17% (average: 1.04%) in interval A, and from 0.05% to 5.04% (average: 1.23%) in interval CPE, respectively. Please refer to Supplementary Materials.

#### 4.3. Inorganic Elements and Isotopic Results

The Vanadium/(Vanadium + Nickel) [V/(V + Ni)] ratios of intervals A and CPE ranged from 0.73% to 0.82% (average: 0.77%) and from 0.72% to 0.89% (average 0.79%), respectively. The  $U_{\text{EF}}$  values of interval A ranged from 0.63% to 6.63% with an average of 1.94%, and the  $U_{\text{EF}}$  values of interval CPE ranged from 0.58 to 4.21 (ave. 2.32). In interval

A, the ( $\delta^{13}\text{C}_{\text{org}}:\text{P}$ ) ratios ranged from 7.2 to 182, with an average of 84.2 and the ( $\delta^{13}\text{C}_{\text{org}}:\text{P}$ ) ratios ranged from 11.9 to 215.8 (average: 97.9). The degree of pyritization ( $\text{DOP}_{\text{T}}$ ) is generally used to evaluate paleoredox conditions [37]. Interval CPE was characterized by high  $\text{DOP}_{\text{T}}$  values, whereas the negative carbon isotope excursion (NCE) zones had much higher  $\text{DOP}_{\text{T}}$  values than those in interval CPE. The  $\text{DOP}_{\text{T}}$  ratios of interval A and interval CPE varied from 0.01 to 0.59 (average: 0.17) and from 0.01 to 0.67 (ave. 0.20), respectively. In addition, interval A  $\delta^{13}\text{C}_{\text{org}}$  values ranged from  $-27.6\text{‰}$  to  $-23.9\text{‰}$  (average:  $-25.9\text{‰}$ ), and interval CPE values were lower than those of interval A and ranged from  $-28.8\text{‰}$  to  $-25.1\text{‰}$ , with an average of  $-26.9\text{‰}$ . The  $\delta^{34}\text{S}$  values in interval A ( $4.4\text{‰}$  to  $12\text{‰}$ ) were slightly higher than those in interval CPE ( $3\text{‰}$  to  $7.2\text{‰}$ ), with averages of  $7.4\text{‰}$  and  $5.0\text{‰}$ , respectively. However, the  $\delta^{15}\text{N}$  values in interval A ( $3.2\text{‰}$  to  $8.5\text{‰}$ ) were slightly lower than those in interval CPE ( $7.3\text{‰}$  to  $12.2\text{‰}$ ), with averages of  $5.4\text{‰}$  and  $9.4\text{‰}$ , respectively. Please refer to Supplementary Materials.

## 5. Discussion

### 5.1. Pyritization of Chrysophyte Cyst Fossils

Chrysophyte cyst fossils were widely pyritized and preserved in the black shales, together with framboidal pyrite in the Ch7 Mbr of the Yanchang Formation (Figures 5A–C and 6A–D). The six types of chrysophyte cyst fossils are shown in Figure 6E–J, which were discovered in Ch7 black shales in well Zhen421 in this paper. Although similar types of fossils were described by Zhang et al. (2016), more fossil details (such as pyritized walls, fossil interiors, and the inside of collars and walls) are reported in this paper [8]. In this study, chrysophyte cyst fossils were mostly spherical or oval in shape (Figure 6E–J), and the average diameter of the intact cysts was  $10\ \mu\text{m}$  (Figure 6K,L). Chrysophyte cysts were divided into anterior and posterior hemispheres, with pores found in the anterior hemisphere [38,39] (Figure 6K,L). A few cysts had conical pores without collars, whereas most cysts had cylindrical or obconical collars around the pores [39] (Figure 6E–J). The surface ornamentation of the cysts included circuli (Figure 6F), verrucae (Figure 6G), ridges (Figure 6H), reticula (Figure 6I), and stars [8,38] (Figure 6I), whereas some cysts were characterized by no ornamentation (Figure 6E). Constricted cavities were observed between the wall and fossil interior of the chrysophyte cysts (Figure 6M,N). The internal structures of the collars of chrysophyte cysts are shown in Figure 6O–S. The interior characteristics of the collars have different shapes. The chrysophyte cysts had walls with a thickness of  $0.05\ \mu\text{m}$ , and the inside of the wall of some chrysophyte cysts had small and evenly distributed protuberances (Figure 6O–T).

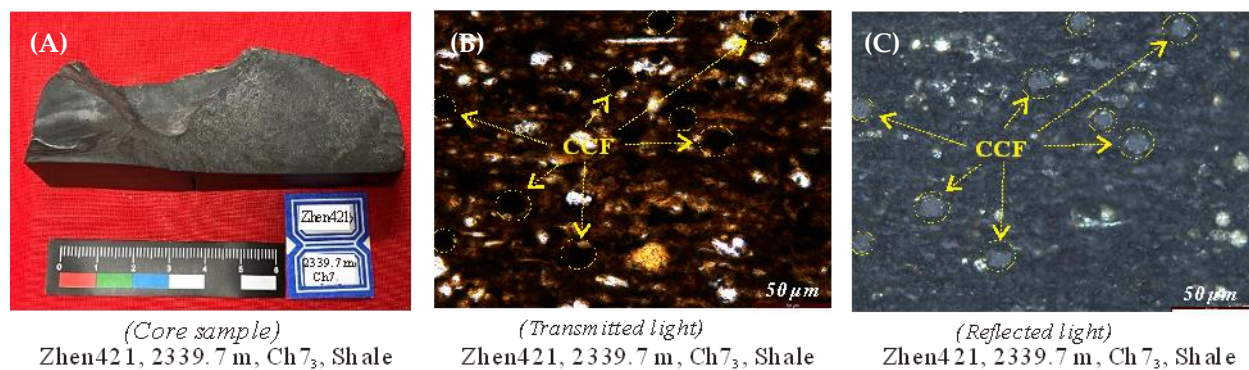


**Figure 5.** Photographs of black shale (A) and thin sections of black shale with chrysophyte cysts under transmitted light (B) and reflected light (C). CCF represents the chrysophyte cyst fossil.

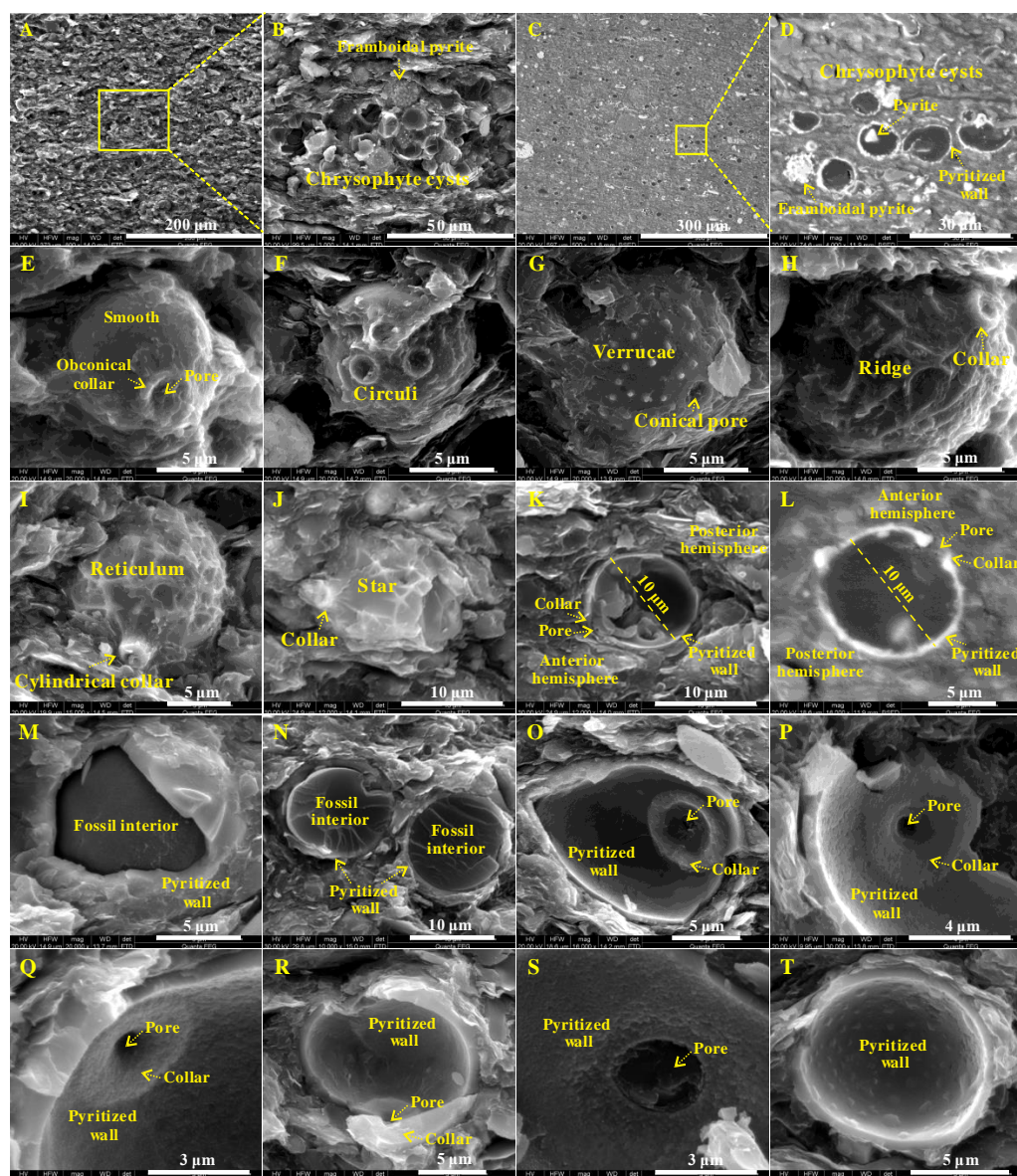


**Figure 6.** SEM images of the chrysophyte cysts in manually broken surfaces (A,B) without polishing and (C,D) polished surfaces in the black shales. The six types of chrysophyte cysts with (E) smooth, (F) circuli, (G) verrucae, (H) ridges, (I) reticula, and (J) stars. Vertical sections of (K) unpolished and (L) polished samples showing internal structures of the chrysophyte cysts. (M,N) Pyritized wall, fossil interior, (O–S) inside of collars, and (T) wall of the chrysophyte cysts in the shales at the bottom of the Ch7 Mbr of the Yanchang Fm. (sample: Zhen421, 2339.7 m, Ch7 Mbr, black shale).

### 5.2. Age of the Chrysophyte Cysts and the Triassic CPE

Ch7 Mbr showed well-preserved Milankovitch cycles [23]. The long eccentricity (E) is the most stable Earth orbit parameter [32]. Thirteen filtered 405 kyr long eccentricity cycles of wells Yan56 and Zhen421 (Gauss filter) were identified (Figure 4A). The floating astronomical scale of Ch7 Mbr was established based on a previous study [23]. The depositional duration of the Ch7 Mbr in the Yanchang Formation was approximately 5 Ma. Furthermore, the U-Pb isotopic age of zircons in the tuffs at the bottom of the Ch7 Mbr was 234 Ma based on La-ICP-MS analysis (Figure 4B), and it served as a geological anchor [33]. The last U-Pb isotopic age of zircons in the lower Ch7 Mbr in the section of Yunmeng and Yishi villages is in agreement with this result (Figure 4B) [33,34]. The ATS of the Ch7 Mbr was determined according to the floating astronomical scale and geological anchors. The depositional ages of three subunits in the Ch7 Mbr were determined at 234.0 Ma to

232.4 Ma (Ch<sub>7</sub> sub-Mbr), 232.4 Ma to 230.8 Ma (Ch<sub>7</sub> sub-Mbr), and 230.8 Ma to 229.1 Ma (Ch<sub>7</sub> sub-Mbr) from the bottom to the top (Figure 7). In this study, according to the ATS, chrysophyte cysts were discovered at the top of E1, with each long eccentricity (E) representing 405 kyr. The microfossils of chrysophyte cysts in the Ch7 Mbr black shales were estimated to be at least 233.6 Ma (Figure 7). Previous studies have indicated that CPE is a period of marked changes in the global climate from 234 Ma to 232 Ma [35,36]. Chrysophyte cysts in the Ch7 Mbr black shales were well preserved during CPE.

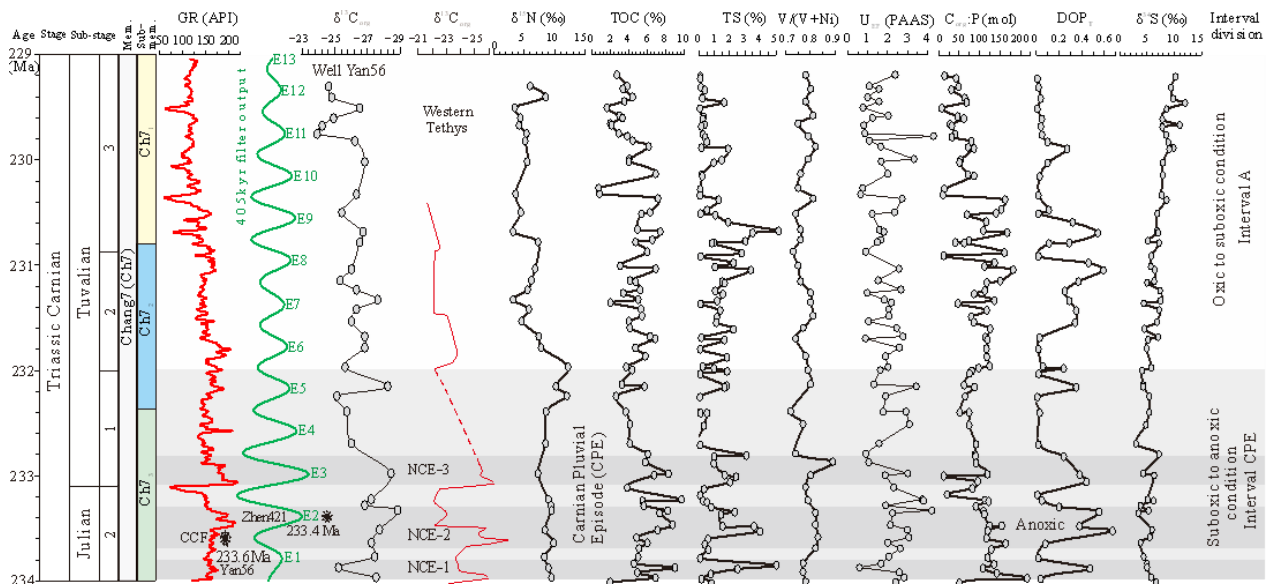


**Figure 7.** Vertical variation of geochemical parameters of the black shales in the Ch7 Mbr from well Yan56, Ordos Basin [24–26,28]. Please refer to Supplementary Materials. NCE represents negative carbon isotope excursion. CCF represents the chrysophyte cyst fossil.

### 5.3. Depositional Response and Redox Conditions in the CPE

During the Triassic CPE, the lake water level reached its maximum because of excessive rainfall and surface runoff [35]. Under these conditions, black organic-rich shales in the Ch7 Mbr were widely deposited, signifying suboxic to anoxic depositional environmental conditions in the global CPE. CPE is characterized by multiple negative carbon isotope excursions [35], increased rainfall [40], intensified continental weathering [41], and widespread anoxic conditions [36,42]. As shown in Figure 7, NCEs in the black shales of the Ch7 Mbr were recorded, which was consistent with the carbon isotope schematic composite curve of the northwestern Tethyan realm in the CPE [35] (Figure 7). In addition, the  $\delta^{34}\text{S}$  values of interval CPE ranged from 3 to 7.2‰, with an average of 5.0‰. The  $\delta^{34}\text{S}$  of seawater in the Late Triassic was generally 15.5‰ [43]. Thus, the  $\delta^{34}\text{S}$  fractionation in the interval CPE varied from 8.3‰ to 12.5‰, suggesting that sulfur originating from atmospheric precipitation and surface runoff varied from 3‰ to 15‰ [44]. The interval CPE of Ch7 Mbr showed indications of strong rainfall and surface runoff. Nitrogen isotopes ( $\delta^{15}\text{N}$ ) act as effective proxies for evaluating redox conditions [45]. Under suboxic conditions, incomplete denitrification (conversion of nitrate to  $\text{N}_2$  gas) resulted in high  $\delta^{15}\text{N}$  values [45,46]. The  $\delta^{15}\text{N}$  values in interval CPE were higher than those in interval A, indicating suboxic-to-anoxic conditions (Figure 7).

Redox-sensitive trace element concentrations and ratios are widely used as indicators of redox conditions [47]. Uranium (U) is highly soluble under oxic conditions, and a high concentration of the U element indicates oxygen-deficient bottom water [47,48]. The interval CPE had higher  $U_{\text{EF}}$  values than interval A under suboxic to anoxic conditions. Vanadium (V) exists as  $\text{V}^{5+}$  (i.e.,  $\text{HVO}_4^{2-}$ ) in vanadate ionic species under oxic conditions, whereas  $\text{V}^{5+}$  is converted to  $\text{V}^{3+}$  in the form of solid oxides or hydroxides under reductive conditions [47]. Elemental V is more concentrated in anoxic environments than nickel

(Ni) [49,50]; therefore, the  $V/(V + Ni)$  ratio was used to evaluate the redox conditions and stratification of bottom water [49]. The  $V/(V + Ni)$  ratios ranged from 0.72% to 0.89% (average: 0.79%) in the interval CPE, indicating suboxic to anoxic conditions with stratified water (Figure 7).

#### 5.4. Models of Preservation of Chrysophyte Cyst Fossils

Based on SEM observations, it was apparent that the chrysophyte cyst fossils were well preserved through pyritization in the black shales of the Ch7 Mbr in the CPE (Figure 8). Although chrysophyte cyst fossils have previously been reported in the Triassic Yanchang Fm. [8], their preservation conditions and pyritization were not studied. In this study, a model was developed to explain the formation mechanism of pyritized fossils. CPE is a key period in global climate change [36,40,51]. Surface runoff leads to high terrigenous detrital matter inputs and enhanced the supply of sulfate in the CPE [24,28,40–42] (Figure 9A). As discussed above, the sulfur in the black shales of the Ch7 Mbr originated from watermass sulfate [25,28]. Chrysophyte cyst fossils were probably pyritized near the water-sediment (W-S) interface in suboxic to anoxic environments (Figure 9B). The two steps of pyritization of chrysophyte cysts are shown in Figure 9C. Pyritization was initiated on the wall of the chrysophyte cysts, with microcrystalline pyrite precipitation (Step 1). Subsequently, full pyritization of the wall was achieved (Step 2) (Figure 9C). Under the above conditions, the organic matter was degraded by anaerobic metabolic processes [52]. Pyrite was formed by the reaction of sulfide ( $H_2S$ ) with reduced iron ( $Fe^{2+}$ ) (Figure 9B).  $H_2S$  was produced via bacterial sulfate reduction (BSR;  $2CH_2O + SO_4^{2-} \rightarrow 2HCO_3^- + H_2S$ ) (Figure 9A), whereas  $Fe^{2+}$  was predominantly released from the reactive iron-bearing minerals [53]. In addition, the organic matter content affected the redox conditions of the bottom water column by affecting the BSR intensity, which in turn regulated pyritization. Our results showed that the interval CPE in Ch7 Mbr had higher average TOC values (5.60 wt.%) than those of interval A. The addition of organic matter enhanced the BSR, which led to an increase in the  $H_2S$  content. According to the EDS results, both chrysophyte cyst fossils and framboidal pyrite were enriched in Fe and S, which exhibited strong reflection under the light (Figure 8A). Initially, pyrite was preferentially formed on the surface of chrysophyte cyst fossils, where the diffusive  $H_2S$  encountered  $Fe^{2+}$  [54,55]. Because the external surface of the chrysophyte cyst was gradually pyritized, the organic matter in the fossil interior was well preserved (Figure 8). The fossil interior was predominantly composed of C and differed in elemental composition from the external surface (Figure 8B–C). Overall, chrysophyte cyst fossils were preserved in the Triassic Ch7 Mbr black shale during the CPE and were substantially pyritized. BSR caused fossil pyritization under suboxic to anoxic conditions, while the high organic matter and supply of sulfate stimulated the BSR process. Thus, fossil pyritization has contributed substantially to fossil preservation.

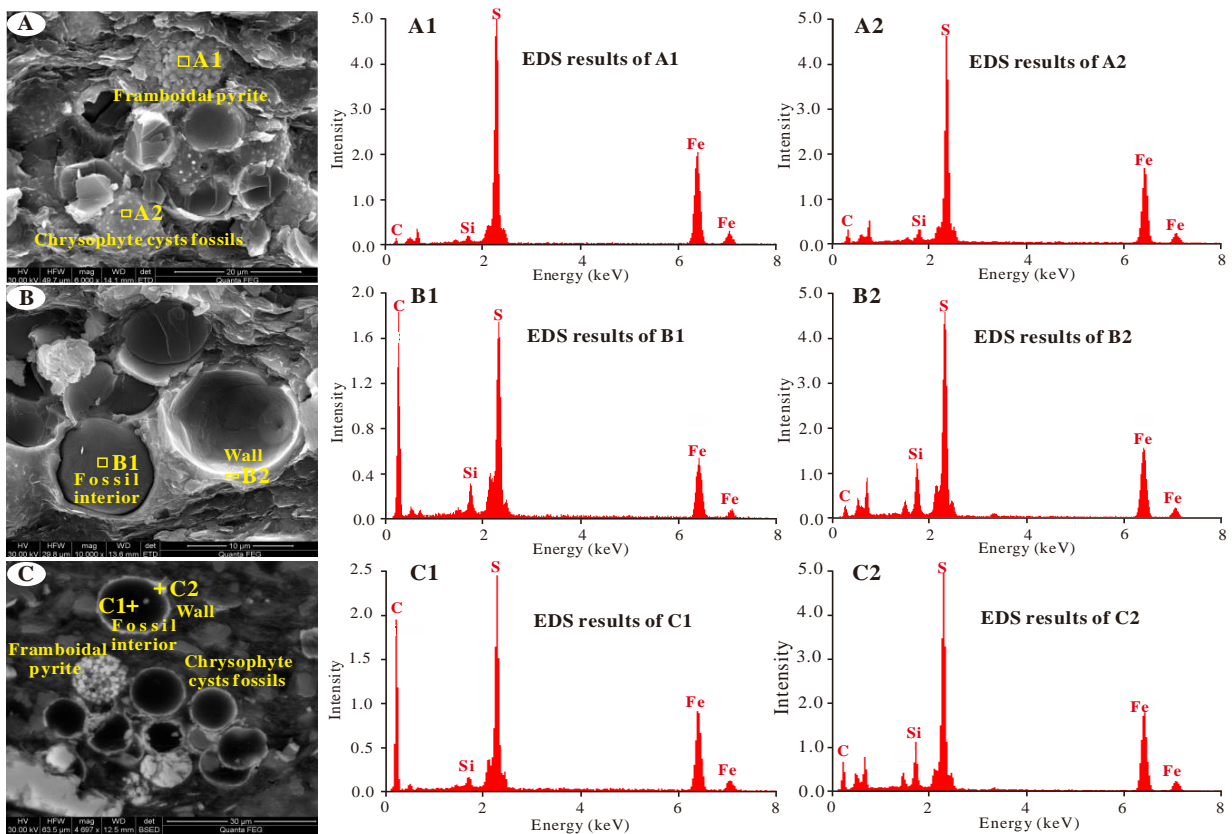


**Figure 8.** (A) SEM images, (A1) EDS results of the chrysophyte cysts, and (A2) framboidal pyrite in the unpolished shales. (B) SEM images, (B1) EDS results of the fossil interior, and (B2) pyritized wall of the chrysophyte cysts in the unpolished shale samples. (C) SEM images, (C1) EDS results of the fossil interior, and (C2) pyritized wall of the chrysophyte cysts in the polished shale samples from Yanchang Fm. (sample: Zhen421, 2339.7 m, Ch7 Mbr, black shale).

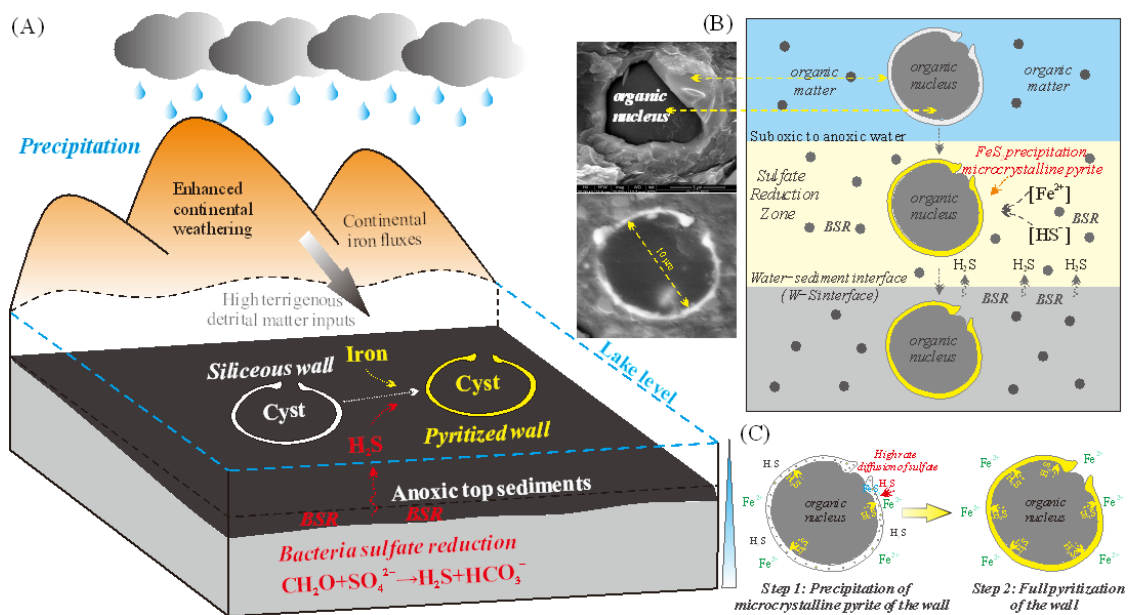


**Figure 9.** (A) A model explaining the preservation of chrysophyte cysts under anoxic conditions in the CPE (modified from Saleh et al., 2018 [56]), (B) fossilization process of chrysophyte cysts in the sulfate reduction zone, and (C) steps of chrysophyte cysts pyritization.

In addition, fossil pyritization and preservation models were studied in different shale basins [56,57]. Saleh et al. provided an orbital-controlled soft-tissue fossilization in Fezouata black shale [56]. Guan et al. revealed the preservation of pyritized *Chuarina* in the Ediacaran shales, dominated by sedimentary organic matter content and bottom water redox condition [57]. However, chrysophyte cysts were characterized by siliceous structures, which were widely distributed in modern lake sediments in southwest Greenland [2], Western United States [3], northern Poland [5], Finland [6], northwestern Mediterranean region [7], Muskoka Haliburton region [9], Northeast Spain [10], and northeast China [39]. But, chrysophyte cyst fossils were first discovered in the Triassic Yanchang Formation, Ordos Basin, China [8]. The pyritization and preservation model of chrysophyte cyst fossils in this study were comprehensively discussed, which provided detailed information on the pyritization and evolution of algae with siliceous structures for the first time.

## 6. Conclusions

Chrysophyte cysts were discovered in the black shales of the Ch7 Mbr in the Yanchang Fm. Although previous studies primarily focused on their morphological characteristics, models of their preservation and pyritization have not been developed. In this study, the ATS of Ch7 Mbr was determined based on cyclostratigraphy and radiometric dating. The tuffs at the bottom of Ch7 Mbr were crystallized in 234 Ma and the duration of Ch7 Mbr was estimated to be approximately 5 Ma. According to the  $^{206}\text{Pb}/^{238}\text{U}$  isotopic age of zircons and cyclostratigraphic analysis, The three subunits in the Ch7 Mbr were deposited at 234.0–232.4 Ma, 232.4–230.8 Ma, and 230.8–229.1 Ma. Moreover, six types of chrysophyte cyst fossils were well pyritized and preserved in the Triassic CPE, and the age of the fossils was at least 233.6 Ma based on the ATS. Models of chrysophyte cyst preservation indicated that BSR led to fossil pyritization near the W-S interface under suboxic to anoxic environments. Pyritization was initiated on the walls of the chrysophyte cysts by the formation of microcrystalline pyrite. Subsequently, the wall was fully pyritized, a fact that contributed to the preservation of organic matter in the fossil interior. Thus, fossil pyritization considerably contributed to their preservation.

**Supplementary Materials:** The following supporting information can be downloaded at: <https://www.mdpi.com/article/10.3390/min13080991/s1>.

**Author Contributions:** J.C.: Formal analysis, writing—original draft; W.G. (corresponding author): supervision, writing—review and editing; S.Y.: supervision, investigation, data curation. All authors have read and agreed to the published version of the manuscript.

**Funding:** This research was funded by PetroChina Changqing Oilfield Company (Grant No. Ji 2021-38).

**Data Availability Statement:** Not Applicable.

**Acknowledgments:** We thank the PetroChina Changqing Oilfield Company for providing the shale samples. We would like to thank the editors and reviewers for their constructive comments.

**Conflicts of Interest:** The authors declare no conflict of interest.

## References

1. Andersen, R.A. Synurophyceae classis nov., a new class of algae. *Am. J. Bot.* **1987**, *74*, 337–353.
2. Pla, S.; Anderson, N.J. Environmental factors correlated with chrysophyte cyst assemblages in low arctic lakes of southwest Greenland. *J. Phycol.* **2005**, *41*, 957–974.
3. Adam, D.P.; Mahood, A.D. Chrysophyte cysts as potential environmental indicators. *GSA Bull.* **1981**, *92*, 839–844.
4. Holen, D.A. Chrysophyte stomatocyst production in laboratory culture and descriptions of seven cyst morphotypes. *Phycologia* **2014**, *53*, 426–432.
5. Hernández-Almeida, I.; Grosjean, M.; Tylmann, W.; Bonk, A. Chrysophyte cyst-inferred variability of warm season lake water chemistry and climate in northern Poland: Training set and downcore reconstruction. *J. Paleolimnol.* **2015**, *53*, 123–138.
6. Korkonen, S.; Weckström, J.; Korhola, A. Biogeography and ecology of freshwater chrysophyte cysts in Finland. *Hydrobiologia* **2020**, *847*, 487–499.
7. Pla, S.; Catalan, J. Chrysophyte cysts from lake sediments reveal the submillennial winter/spring climate variability in the northwestern Mediterranean interval throughout the Holocene. *Clim. Dyn.* **2005**, *24*, 263–278.

8. Zhang, W.Z.; Yang, H.; Xia, X.Y.; Xie, L.Q.; Xie, G.W. Triassic chrysophyte cyst fossils discovered in the Ordos Basin, China. *Geology* **2016**, *44*, 1031–1034.
9. Wilkinson, A.N.; Hall, R.I.; Smol, J.P. Chrysophyte cysts as paleolimnological indicators of environmental change due to cottage development and acidic deposition in the Muskoka-Haliburton interval, Ontario, Canada. *J. Paleolimnol.* **1999**, *22*, 17–39.
10. Pla, S.; Camarero, L.; Catalan, J. Chrysophyte cyst relationships to water chemistry in Pyrenean lakes (NE Spain) and their potential for environmental reconstruction. *J. Paleolimnol.* **2003**, *30*, 21–34.
11. Zhao, G.C.; Sun, M.; Wilde, S.A.; Li, S.Z. Late Archean to Paleoproterozoic evolution of the North China Craton: Key issues revisited. *Precambrian Res.* **2005**, *136*, 177–202.
12. Yang, H.; Deng, X. Deposition of Yanchang Formation deep-water sandstone under the control of tectonic events in the Ordos Basin. *Petrol. Explor. Dev.* **2013**, *40*, 549–557.
13. Zou, C.; Wang, L.; Li, Y.; Tao, S.; Hou, L. Deep-lacustrine transformation of sandy debrites into turbidites, Upper Triassic, Central China. *Sediment. Geol.* **2012**, *265*, 143–155.
14. Zhang, W.Z.; Yang, W.W.; Xie, L.Q. Controls on organic matter accumulation in the triassic Chang 7 lacustrine shale of the Ordos Basin, central China. *Int. J. Coal Geol.* **2017**, *183*, 38–51.
15. Guo, H.; Jia, W.; Peng, P.A.; Lei, Y.; Luo, X.; Cheng, M.; Wang, X.; Zhang, L.; Jiang, C. The composition and its impact on the methane sorption of lacustrine shales from the Upper Triassic Yanchang Formation, Ordos Basin, China. *Mar. Petrol. Geol.* **2014**, *57*, 509–520.
16. Liu, H.L.; Zou, C.N.; Qiu, Z.; Pan, S.Q.; Zhang, W.Z.; Jing, Z.H.; Hao, J.H.; Wu, S.T.; Li, S.X.; Guo, Q.L. Sedimentary enrichment factors of extraordinarily high organic matter in the sub-member 3 of Member 7 of Yanchang Formation, Ordos Basin. *Acta Petroli Sin.* **2022**, *43*, 1520–1541.
17. Zhang, W.Z.; Yang, H.; Yang, W.W.; Wu, K.; Liu, F. Assessment of geological characteristics of lacustrine shale oil reservoir in Chang7 Member of Yanchang Formation, Ordos Basin. *Geochimica* **2015**, *44*, 505–515.
18. Yang, S.R.; Gang, W.Z.; Cao, J.J.; Liu, J.P.; Gao, G.; Dang, W.L. Geochemical characteristics, origin and carbon isotope reversal of the presalt natural gas in the Lower Paleozoic Ordovician carbonates, Ordos Basin, China. *Mar. Petrol. Geol.* **2022**, *139*, 105577.
19. Chen, G.; Gang, W.Z.; Liu, Y.Z.; Wang, N.; Guo, Y.; Zhu, C.Z.; Cao, Q.Y. High-resolution sediment accumulation rate determined by cyclostratigraphy and its impact on the organic matter abundance of the hydrocarbon source rock in the Yanchang Formation, Ordos Basin, China. *Mar. Petrol. Geol.* **2019**, *103*, 1–11.
20. Schnyder, J.; Ruffell, A.; Deconinck, J.F.; Baudin, F. Conjunctive use of spectral gamma-ray logs and clay mineralogy in defining late Jurassic–early Cretaceous palaeoclimate change (Dorset, U.K.). *Palaeogeogr. Palaeoclimatol.* **2006**, *229*, 303–320.
21. Li, M.S.; Hinnov, L.A.; Huang, C.J.; Ogg, J.G. Sedimentary noise and sea levels linked to land–ocean water exchange and obliquity forcing. *Nat. Commun.* **2018**, *9*, 1004. [[CrossRef](#)]
22. Wu, H.C.; Zhang, S.L.; Huang, Q.H. Establishment of floating astronomical time scale for the terrestrial Late Cretaceous Qingshankou Formation in the Songliao Basin of Northeast China. *Ear. Sci. Front.* **2008**, *15*, 159–169. [[CrossRef](#)]
23. Zhang, R.; Jin, Z.J.; Liu, Q.Y.; Li, P.; Huang, Z.K.; Shi, J.Y.; Ge, Y.J.; Du, K.F. Astronomical constraints on deposition of the Middle Triassic Chang 7 lacustrine shales in the Ordos Basin, Central China. *Palaeogeogr. Palaeoclimatol.* **2019**, *528*, 87–98. [[CrossRef](#)]
24. Yuan, W.; Liu, G.D.; Bulseco, A.; Zhou, X.X. Iron speciation in organic-rich shales from the Upper Triassic Yanchang Formation, Ordos Basin, Northern China: Implications for depositional environment. *J. Asian Earth Sci.* **2021**, *220*, 104917.
25. Chen, G.; Chang, X.C.; Gang, W.Z.; Wang, N.; Zhang, P.F.; Cao, Q.Y.; Xu, J.B. Anomalous positive pyrite sulfur isotope in lacustrine black shale of the Yanchang Formation, Ordos Basin: Triggered by paleoredox chemistry changes. *Mar. Petrol. Geol.* **2020**, *121*, 104587. [[CrossRef](#)]
26. Chen, R.Q.; Liu, G.D.; Shang, F.; Cao, Y.S. Nitrogen isotope compositions of the Upper Triassic Chang 7 Shale, Ordos Basin, North China: Implications for depositional redox conditions. *Mar. Petrol. Geol.* **2019**, *109*, 279–290. [[CrossRef](#)]
27. Yang, S.R.; Gao, G.; Liu, Y.; Gang, W.Z.; Dang, W.L. Organic geochemistry and petrographic characteristics of the shales from the Late Miocene Zeit Formation in the Tokar area, Red Sea Basin: Implications for depositional environment and hydrocarbon potential. *J. Petrol. Sci. Eng.* **2020**, *199*, 107757. [[CrossRef](#)]
28. Chen, R.Q.; Liu, G.D.; Shang, F.; Cao, Y.S. Variations in hydrocarbon generating potential of the Chang 7 shale: Evidence from pyrite morphology and sulfur isotope. *J. Petrol. Sci. Eng.* **2020**, *195*, 107747. [[CrossRef](#)]
29. Li, X.; Gang, W.; Yao, J.; Gao, G.; Wang, C.; Li, J.; Liu, Y.; Guo, Y.; Yang, S. Major and trace elements as indicators for organic matter enrichment of marine carbonate rocks: A case study of Ordovician subsalt marine formations in the central-eastern Ordos Basin, North China. *Mar. Petrol. Geol.* **2020**, *111*, 461–475.
30. Hu, Y.; Feng, D.; Peckmann, J.; Roberts, H.H.; Chen, D.F. New insights into cerium anomalies and mechanisms of trace metal enrichment in authigenic carbonate from hydrocarbon seeps. *Chem. Geol.* **2014**, *381*, 55–66. [[CrossRef](#)]
31. Taylor, S.R. *The Continental Crust: Its Composition and Evolution: An Examination of the Geochemical Record Preserved in Sedimentary Rocks*; Blackwell Scientific Publications: Palo Alto, CA, USA, 1985; p. 328.
32. Laskar, J.; Robutel, P.; Joutel, F.; Gastineau, M.; Correia, A.C.M.; Levrard, B. A long-term numerical solution for the insolation quantities of the Earth. *Astron. Astrophys.* **2004**, *428*, 261–285. [[CrossRef](#)]
33. Sun, Y.W.; Li, X.; Liu, Q.Y.; Zhang, M.D.; Li, P.; Zhang, R.; Shi, X. In search of the inland Carnian Pluvial Event: Middle–Upper Triassic transition profile and U–Pb isotopic dating in the Yanchang Formation in Ordos Basin, China. *Geol. J.* **2019**, *55*, 4905–4919. [[CrossRef](#)]

34. Zhu, R.K.; Cui, J.W.; Deng, S.H.; Luo, Z.; Lu, Y.Z.; Qiu, Z. High-precision Dating and Geological Significance of Chang 7 Tuff Zircon of the Triassic Yanchang Formation, Ordos Basin in Central China. *Acta. Geol. Sin.-Engl. Ed.* **2019**, *93*, 1823–1834. [[CrossRef](#)]
35. Dal Corso, J.; Gianolla, P.; Rigo, M.; Franceschi, M.; Roghi, G.; Mietto, P.; Manfrin, S.; Raucsik, B.; Budai, T.; Jenkyns, H.C.; et al. Multiple negative carbon-isotope excursions during the Carnian Pluvial Episode (Late Triassic). *Earth-Sci. Rev.* **2018**, *185*, 732–750. [[CrossRef](#)]
36. Lu, J.; Zhang, P.X.; Dal Corso, J.; Yang, M.F.; Wignall, P.B.; Greene, S.E.; Shao, L.Y.; Lyu, D.; Hilton, J. Volcanically driven lacustrine ecosystem changes during the Carnian Pluvial Episode (Late Triassic). *Proc. Natl. Acad. Sci. USA.* **2021**, *118*, e2109895118. [[CrossRef](#)]
37. Raiswell, R.; Canfield, D.E. Sources of iron for pyrite formation in marine sediments. *Am. J. Sci.* **1998**, *298*, 219–245. [[CrossRef](#)]
38. Wilkinson, A.N.; Zeeb, B.A.; Smol, J.P. *Atlas of Chrysophycean Cysts Vol. II*; Kluwer Academic Publishers: Dordrecht, The Netherlands, 2001; pp. 1–169.
39. Pang, W.T. *Studies on Chrysophycean Stomatocysts from the Wetlands in Great Xing'an Mountains, China*; East China Normal University: Shanghai, China, 2012; pp. 23–28.
40. Simms, M.J.; Ruffell, A.H. Synchronicity of climatic change and extinctions in the Late Triassic. *Geology* **1989**, *17*, 265–268. [[CrossRef](#)]
41. Dal Corso, J.; Gianolla, P.; Newton, R.J.; Franceschi, M.; Roghi, G.; Caggiati, M.; Raucsik, B.; Budai, T.; Haas, J.; Preto, N. Carbon isotope records reveal synchronicity between carbon cycle perturbation and the “Carnian Pluvial Event” in the Tethys realm (Late Triassic). *Glob. Planet. Change* **2015**, *127*, 79–90. [[CrossRef](#)]
42. Sun, Y.D.; Wignall, P.B.; Joachimski, M.M.; Bond, D.P.G.; Grasby, S.E.; Lai, X.L.; Wang, L.N.; Zhang, Z.T.; Sun, S. Climate warming, euxinia and carbon isotope perturbations during the Carnian (Triassic) crisis in South China. *Earth Planet. Sci. Lett.* **2006**, *444*, 88–100. [[CrossRef](#)]
43. Boschetti, T.; Cortecchi, G.; Toscani, L.; Iacumin, P. Sulfur and oxygen isotope compositions of upper Triassic sulfates from northern Apennines (Italy): Palaeogeographic and hydrogeochemical implications. *Geol. Acta* **2011**, *9*, 129–147.
44. Canfield, D.E. Biogeochemistry of sulfur isotopes. In *Stable Isotope Geochemistry*; Valley, J.W., Cole, D., Eds.; Mineralogical Society of America and Geochemical Society, Reviews of Mineralogy and Geochemistry: Washington, DC, USA, 2001; Volume 43, pp. 607–636.
45. Quan, T.M.; Adigwe, E.N.; Riedinger, N.; Puckette, J. Evaluating nitrogen isotopes as proxies for depositional environmental conditions in shales: Comparing Caney and Woodford Shales in the Arkoma Basin, Oklahoma. *Chem. Geol.* **2013**, *360–361*, 231–240. [[CrossRef](#)]
46. Talbot, M.R. Nitrogen isotopes in palaeolimnology. In *Tracking Environmental Change Using Lake Sediments. Volume 2: Physical and Geochemical Methods*; Last, W.M., Smol, J.P., Eds.; Kluwer Academic Publishers: Dordrecht, The Netherlands, 2001; pp. 401–439.
47. Algeo, T.J.; Maynard, J.B. Trace–element behavior and redox facies in core shales of Upper Pennsylvanian Kansas–type cyclothems. *Chem. Geol.* **2004**, *206*, 289–318. [[CrossRef](#)]
48. Tribouvillard, N.; Algeo, T.J.; Lyons, T.; Riboulleau, A. Trace–metals as paleoredox and paleoproductivity proxies: An update. *Chem. Geol.* **2006**, *232*, 12–32. [[CrossRef](#)]
49. Hatch, J.R.; Leventhal, J.S. Relationship between inferred redox potential of the depositional environment and geochemistry of the Upper Pennsylvanian (Missourian) Stark Shale Member of the Dennis Limestone, Wabaunsee County, Kansas, USA. *Chem. Geol.* **1992**, *99*, 65–82. [[CrossRef](#)]
50. Jones, B.; Manning, D.A.C. Comparison of geochemical indices used for the interpretation of palaeoredox conditions in ancient mudstones. *Chem. Geol.* **1994**, *111*, 111–129. [[CrossRef](#)]
51. Dal Corso, J.; Bernardi, M.; Sun, Y.D.; Song, J.J.; Seyfullah, L.J.; Preto, N.; Gianolla, P.; Ruffell, A.; Kustatscher, E.; Roghi, G.; et al. Extinction and dawn of the modern world in the Carnian (Late Triassic). *Sci. Adv.* **2020**, *6*, eaba0099. [[CrossRef](#)]
52. Canfield, D.E. Factors influencing organic carbon preservation in marine sediments. *Chem. Geol.* **1994**, *114*, 315–329. [[CrossRef](#)]
53. Canfield, D.E.; Thamdrup, B. Towards a consistent classification scheme for geochemical environments, or, why we wish the term “suboxic” would go away. *Geobiology* **2009**, *7*, 385–392. [[CrossRef](#)]
54. Stockdale, A.; Davison, W.; Zhang, H. Formation of iron sulfide at faecal pellets and other microniches within suboxic surface sediment. *Geochim. Cosmochim. Acta* **2010**, *74*, 2665–2676. [[CrossRef](#)]
55. Xiao, S.; Schiffbauer, J.D.; McFadden, K.A.; Hunter, J. Petrographic and SIMS pyrite sulfur isotope analyses of Ediacaran chert nodules: Implications for microbial processes in pyrite rim formation, silicification, and exceptional fossil preservation. *Earth Planet. Sci. Lett.* **2010**, *297*, 481–495. [[CrossRef](#)]
56. Saleh, F.; Pittet, B.; Perrillat, J.P.; Lefebvre, B. Orbital control on exceptional fossil preservation. *Geology* **2019**, *47*, 103–106. [[CrossRef](#)]
57. Guan, C.; Wang, W.; Zhou, C.; Muscente, A.D.; Wan, B.; Chen, X.; Yuan, X.; Chen, Z.; Ouyang, Q. Controls on fossil pyritization: Redox conditions, sedimentary organic matter content, and Chuaria preservation in the Ediacaran Lantian Biota. *Palaeogeogr. Palaeoclim. Palaeoecol.* **2017**, *474*, 26–35. [[CrossRef](#)]

**Disclaimer/Publisher’s Note:** The statements, opinions and data contained in all publications are solely those of the individual author(s) and contributor(s) and not of MDPI and/or the editor(s). MDPI and/or the editor(s) disclaim responsibility for any injury to people or property resulting from any ideas, methods, instructions or products referred to in the content.